Evidence of abrupt transitions between sea ice dynamical regimes in the East Greenland marginal ice zone

Daniel M. Watkins[1], Angela C. Bliss[2], Jennifer K. Hutchings[3], Monica M. Wilhelmus[1]

[1]Center for Fluid Mechanics, School of Engineering, Brown University, Providence, RI
[2]Cryospheric Sciences Laboratory, NASA Goddard Space Flight Center, Greenbelt, MD
[3]College of Earth, Ocean, and Atmospheric Sciences, Oregon State University, Corvallis, OR

Key Points:

- Ice dynamics measured with two new Lagrangian datasets show strong bathymetry dependent differences over short spatial scales
- Wind variability is insufficient to describe drift speed variability in regions with abrupt changes in bathymetry
- Models that neglect small-scale ocean variability will systematically underestimate ice deformation in the Greenland Sea and Fram Strait

Corresponding author: Monica M. Wilhelmus, mmwilhelmus@brown.edu

Abstract

Sea ice modulates the energy exchange between the atmosphere and the ocean through its kinematics. Marginal ice zone (MIZ) dynamics are complex and are not well resolved in routine observations. Here, we investigate sea ice dynamics in the Greenland Sea MIZ using *in situ* and remote sensing Lagrangian drift datasets. These datasets provide a unique view into ice dynamics spanning spatial scales. We find evidence of tidal currents strongly affecting sub-daily sea ice motion. Velocity anomalies show abrupt transitions aligned with gradients in seafloor topography, indicating changes in ocean currents. Remote-sensed ice floe trajectories derived from moderate resolution satellite imagery provide a view of small-scale variability across the Greenland continental shelf. Ice floe trajectories reveal a west-east increasing velocity gradient imposed by the East Greenland Current, with maximum velocities aligned along the continental shelf edge. These results highlight the importance of small scale ocean variability for ice dynamics in the MIZ.

Plain Language Summary

Sea ice in the Arctic Ocean plays an important role in climate due to its influence on ocean circulation and air-sea energy exchange. Ice motion results from competing and interacting effects of winds, ocean currents, and internal ice stresses. This study uses two novel observational datasets to analyze ice motion in the Greenland Sea and Fram Strait marginal ice zones. We find abrupt changes in the primary causes of ice motion associated with seafloor topography. In shallow seas, strong tidal currents affect ice drift, resulting in repeated opening and closing of the ice. Near the shelf edge, boundary currents increase ice drift speeds, causing ice pack shear. Sea ice models that ignore small-scale ocean currents will underestimate ice deformation.

1 Introduction

The Arctic is warming at over twice the rate of the global average as a result of rising greenhouse gas concentrations (Taylor et al., 2022). A hallmark of Arctic change is a thinning and retreating ice pack (Maslanik et al., 2007; Comiso et al., 2017). Areas of sea ice decline are seeing stronger momentum transfer to the ocean (Polyakov et al., 2020), intensifying ocean eddies (Manucharyan et al., 2022), amidst other effects (Feldl et al., 2020). Furthermore, previously ice-bound sea routes have rising ship traffic as the ice edge moves northward (Boylan, 2021; Dawson et al., 2018), increasing the potential need for accurate drift forecasts.

Quantifying the dynamics of sea ice in the MIZ has been an ongoing challenge (Dumont, 2022). In situ sea ice motion measurements are primarily retrieved from moorings and drifting buoys. These instruments are difficult to deploy and generally exhibit a low residence time in MIZ. As a result, there are rarely multiple buoys in the MIZ at any given time. Remote sensing campaigns have been an invaluable complement, but the low data acquisition rate (on the order of days) inherently limits the physical processes being resolved (Kwok, 2010). Sea ice dynamics at sub-daily time scales, for instance, are important for measuring the lead opening rate and ridging (Hutchings et al., 2011), key parameters for modeled sea ice growth and air-ocean fluxes. Ice motion in the MIZ is tightly coupled to ocean variability at small and moderate length and time scales, including eddies (Manucharyan et al., 2022), boundary currents (Quadfasel et al., 1987), and tidal currents (Heil et al., 2008; Vasulkar et al., 2022).

This study aims to characterize marginal ice dynamics in the Eastern Greenland Coast and the Fram Strait region across a broad range of scales. To this end, we leverage two new observational datasets, each providing Lagrangian measures of ice motion: buoy drift trajectories from the Multidisciplinary drifting Observatory for the Study of Arctic Climate (MOSAiC, Nicolaus (2022)) and ice floe trajectories obtained from mod-

erate resolution remote sensing imagery via the Ice Floe Tracker algorithm (IFT, (Lopez-Acosta et al., 2019)). The MOSAiC drift trajectories represent the highest density of in situ ice dynamics observations yet collected. During the summer period investigated here, up to 80 instruments are reporting simultaneously in a region that rarely has more than 2 instruments present. Ice floe trajectories from IFT allow investigation of variation in ice motion at high resolution, as the motion of individual ice floes is measured rather than the area-averaged velocity that is provided by traditional remote-sensing velocity products.

2 Data and Methods

2.1 MOSAiC Drift Trajectories

Drift trajectories (n=108) from sea ice buoys deployed during the Multidisciplinary drifting Observatory for the Study of Arctic Climate (MOSAiC) Expedition were selected such that trajectories (a) contained at least 30 days of data between May 1st and September 1st 2020, (b) had sampling rates of twice hourly or faster, and (c) drifted through the Fram Strait. Buoys were deployed in an array surrounding an instrumented Central Observatory (CO) (Krumpen & Sokolov, 2020; Nicolaus, 2022). Distance between buoys in the MOSAiC Distributed Network (DN, red lines in Figure 1) ranged from less than 1 to 60 km from the CO on May 1st. Nine additional buoys in the Extended Distributed Network (ExDN, gold trajectories in Figure 1) were between 150 and 530 km away from the CO. Positions were interpolated to a 1-hour grid using cubic splines following de-spiking. Drift velocity was computed using centered differences after projecting buoy positions onto the NSIDC north Polar Stereographic grid. Sea ice concentration from AMSR2 (Meier et al., 2018) was interpolated to individual buoy positions to find the latest date where the buoy remains in sea ice. Hourly 10-m wind velocity from the ERA5 reanalysis (Hersbach et al., 2020) was interpolated to buoy and ice floe coordinates. Bathymetry data was obtained from the International Bathymetric Chart of the Arctic Ocean version 4.1 (Jakobsson et al., 2020). Observations at the DN are summarized via median and percentiles for robustness against outliers and to avoid making assumptions about the shape of the distribution.

2.2 Ice Floe Tracker algorithm

The Floe Tracker algorithm (Lopez-Acosta et al., 2019) was used to identify and track sea ice floes in 250 m resolution optical imagery from the Moderate Resolution Imaging Spectroradiometer (MODIS) spanning the spring-to-summer transition from 2003 to 2020. Corrected-reflectance MODIS imagery was downloaded from NASA Worldview (`https://worldview.earthdata.nasa.gov`). Daytime MODIS images from both Aqua and Terra satellites were analyzed and assigned timestamps using the SOIT utility (Hatcher et al., 2022). Both Aqua and Terra provide daily observations, with time offsets between the two satellite images of between 20 and 90 minutes. Floe trajectories were resampled to daily resolution prior to calculating daily displacement, with gaps of at most 1 day in length filled by linear interpolation. In total, drift trajectories (2-60 days) are available from 7,186 floes; median trajectory length is 8 days, and the total number of estimated drift displacements is 51,867.

2.3 Frequency analysis

Rotary spectral analysis was performed using the University of Hawaii PyCurrents Python library (`https://currents.soest.hawaii.edu/hg/pycurrents/`). Velocities for 20-day trajectory segments were de-trended by removing the centered 35-hour mean, filtered with a Hann window. Resulting spectra were then smoothed with a 3-point box-

car filter. Note that while changing the size of the de-trending window affects the magnitude of the spectra for lower frequencies, it does not alter the position of spectral peaks.

The contributions of diurnal and semi-diurnal tides to the sea ice velocity were determined from harmonic analysis as in Pease et al. (1995). The harmonic model has the form

$$X`(t) = C + Dt + \sum_{k=1}^{6} A_k \cos\omega_k t + B_k \sin\omega_k t + \epsilon(t) \ , \tag{1}$$

where $X'(t) = X - \overline{X}$ is the position anomaly centered 35-hour mean, t is the time, C, D, A_k, and B_k are unknowns, and ω_k are the frequencies of the O1, K1, N2, M2, and S2 tidal constituents. The model is solved for each stereographic position component separately. Maximum tidal currents were estimated using centered differences on the predicted position anomalies. Model fit was evaluated with the coefficient of determination.

2.4 Deformation analysis

The horizontal deformation of sea ice was computed via the Green's Theorem method (Hutchings et al., 2012, 2018).

Strain rates were estimated using sets of buoy arrays manually identified from buoy positions on the first of the month (00:00 UTC) and filtered with a 5-km spatial filter. Arrays of three or four buoys were selected to provide full, non-overlapping coverage of the sea ice while reducing the occurrence of skinny triangles leading to inaccurate strain rate estimates. As a result, 80, 74, and 70 arrays were produced for May, June, and July, respectively. Hourly strain rates were computed for each individual array during the month in which the array configuration was defined, and a time series was constructed by appending the mean strain rate components (divergence and maximum shear) across all arrays for each month. Strain rates were not computed following breakup of the CO on 31 July 2020. The mean deformation rate was computed as an area weighted mean to account for variation in array size across the DN.

3 Overview of MOSAiC summer drift

From May to September, 2020, the MOSAiC Distributed Network (DN) transitioned from central Arctic pack ice, through the Fram Strait, and into the East Greenland Current, with most buoys eventually exiting the MIZ into the Greenland Sea (Figure 1, left panel; for place names, see Figure 4, panel e). Drift characteristics vary as the array moves over bathymetric features. We approximate the transition times in the following paragraphs by providing the dates for buoy 2020P225, which was deployed near the Central Observatory; note that the DN had an effective radius of ≈ 60 km, so crossing an underwater feature such as a shelf edge at a constant speed of 0.2 m/s takes nearly 7 days. During the initial stage, the array remained in pack ice over the Nansen Basin (May 1st to June 13th, Figure 1). Drift speeds were low (median speed 7 cm/s) except for the second week of May, coinciding with a strong cyclone. This event induced deformation in the array that peaked at the time of maximum wind speed.

As the array drifted over the Yermak Plateau (June 13-July 12), drift speed increases up to 14 cm/s. Deformation rates began to increase as the first few buoys moved into a shallower region. The ensemble median drift speed anomaly increased as the array drifted over the plateau boundary displaying an apparent diurnal oscillation. Note that the wind speed was not noticeably different from that of the previous month, suggesting the importance of ocean forcing. Both divergence and shear increased at this time. Divergence, like the sub-daily velocity, showed a diurnal oscillation pattern. The oscillation is evidence of working leads repeatedly opening and closing. The periodic changes in divergence preceded the oscillation in the median drift speed anomaly, hinting at the role of internal ice stresses inducing deformation.

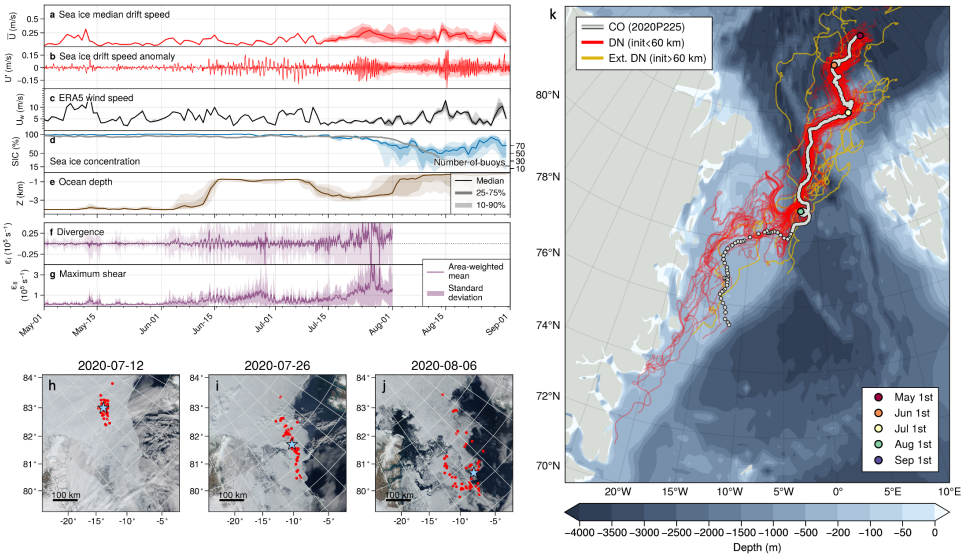

Figure 1. Top left: (a-e) Ensemble distribution of daily medians of observations and conditions for the Distributed Network. Lines indicate ensemble median, while dark and light shading represents the interquartile range and interdecile range respectively. Time series from top to bottom are (a) daily median drift speed, (b) drift speed anomaly (residual after removing daily median speed), (c) ERA5 wind speed, (d) sea ice concentration, (e) ocean depth at buoy positions. Wind speed, depth, and sea ice concentration are interpolated to buoy positions. Observations with estimated sea ice concentration less than 15% were masked prior to calculating percentiles. Panels (f) and (g) show area-weighted means (solid lines) and standard deviations (shading) of divergence and maximum total shear strain rates. Lower left: Buoy positions and sea ice conditions on July 12th (h), July 26th (i), and August 6th (j). The blue star marks the location of 2020P225, which was located at the Central Observatory. Imagery from MODIS accessed through NASA WorldView. Right: Drift trajectories for buoys within the Distributed Network (red) and additional buoys (gold) overlaid on ocean bathymetry. The light gray trajectory corresponds to buoy 2020P225 as in panels (h-j). The dashed portion of the trajectory is when the buoy is on the ice edge and AMSR2 reports 0% sea ice concentration. Colored circles mark the first day of each month.

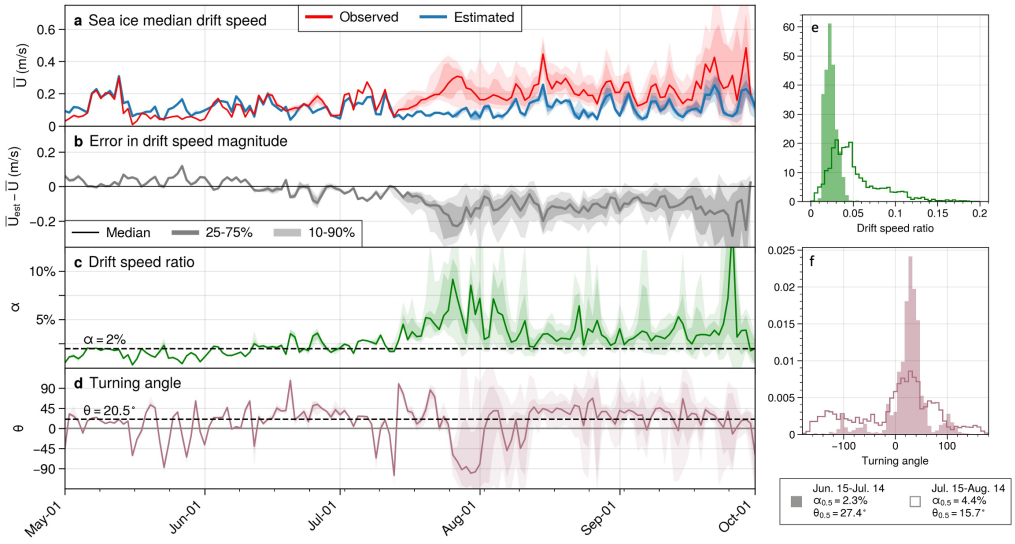

Figure 2. Left: (a) Observed daily median drift speed (red) compared to estimated drift speed (blue), (b) residual of drift speed magnitude, (c) drift speed ratio, (d) turning angle. Solid lines show the ensemble median, and dark and light shading shows the 25-75% and 10-90% ranges. Dashed lines in (b) and (c) mark the May-August median values of the drift speed ratio and turning angles. Right: Histogram estimates of probability density functions for drift speed ratio (e) and turning angle (f). Shaded and outlined distributions summarize the 30 day periods prior to and following July 15th, respectively.

From July 12-August 1 the buoy array drifted southward within the East Greenland Channel and experienced widespread positive divergence and increasing shear, stretching the array on roughly a north-south axis (Figure 1 in panel h and i). Prior to this point, the structure of the deployment array had not undergone significant changes. Sea ice concentration decreased markedly, and we see an increase in 12-hourly oscillations relative to the daily median. Wind speeds were lowest during this period, indicating that the increase in drift speeds must have come from either decreased ice stresses or increased ocean forcing.

Deteriorating ice conditions (Figure 1, panel j) led to the decision at the end of July to dismantle the CO and retrieve many of the autonomous sensors. By August 1st the main floe had broken apart. A portion of the remaining array drifted southeast and appeared to be drawn into a large eddy, while the rest of the array drifted southwest onto East Greenland Shelf (Figure 1 panels j, k). The late summer ice pack comprised distinct floes among patches of open water. The proximity of filaments of sea ice drawn into vortices indicates the presents of mesoscale ocean eddies. A mid-August storm lead to a spike in drift speeds and was followed by enhanced sub-daily, oscillatory variability. By the end of August, all but 12 buoys had drifted into ice-free waters or ceased operation.

4 Relationship between wind and ice velocity at daily timescales

The majority of daily to monthly sea ice drift variability in the central Arctic can be explained by variability in the wind (e.g., Thorndike and Colony (1982)). Thus mo-

tivated, we begin by assuming a simple relationship between ice and wind

$$U = \alpha \exp(\mathrm{i}\theta) U_w + \epsilon \tag{2}$$

where $U = u + iv$ is the complex drift speed, α is a transfer coefficient, which we refer to as the drift speed ratio, θ is the turning angle, $U_w = u_w + iv_w$ is the complex wind speed, and ϵ is the residual. The residual ϵ includes effects of ocean currents, sea surface slope, and internal ice stresses. Changes in ϵ provide an indicator of changes in the key forcings for ice motion. The median drift speed ratio over the study period is $\alpha = 0.021$ and the median turning angle is 20°, in line with previous Arctic Ocean-wide estimates (Brunette et al., 2022, e.g.). Applying these values to Eq. 2 results in the estimated wind speed U_{est} depicted in Figure 2, panel a.

The wind model tends to overestimate the drift speed slightly from May to early June. Thereafter, $\epsilon = |U - U_{est}|$ grows, as does variability in U. The closest agreement to the theoretical value comes when wind speeds are high, (e.g. during the storm in early May), suggesting that the ice approaches free drift during these events. Sustained low wind speeds in mid-to-late July coincided with increased ϵ. Following July 15th, α becomes strongly right-skewed and the median value increases; meanwhile, median θ is close to the same but the likelihood of large deviations increases. Given the low sea ice concentration in the region (Figure 1 panels i, j), it is unlikely that the deviations are due to increases in ice stress. Rather, we surmise that ocean forcing is playing a larger role in ice dynamics from mid-July onward.

The number of buoys decreases as the drift proceeds onto the Greenland Shelf. To supplement the investigation of ice drift variability in the shelf region we turn to the Ice Floe Tracker (IFT). The majority of IFT observations are from the East Greenland Shelf between 70 and 80 N (Figure 3 panel a). Low drift speeds along the coast are the result of frequently occurring landfast ice. Drift speeds are enhanced along the shelf boundary. For most of the region, this area of enhanced drift speed is also the ice edge. Further north, in the East Greenland Channel, we find local maxima in drift speed away from the ice edge along the shelf boundary. Drift direction, too, tends to follow the shelf boundary. On the northwest corner of the shelf, we see some evidence of a re-circulation pattern with northward flow along the coast turning clockwise to join the southward flow, consistent with model results from (Richter et al., 2018).

Empirical estimates of the distribution of turning angles and drift speed ratios for the 20 years of summer IFT data (Figure 3) indicate that both quantities are highly variable and depend on the wind speed. The turning angle distribution for the IFT data is bimodal. Peaks in the θ distribution correspond to the expected 20 degree turning angle and to the reverse of the wind direction. The ice nearly always moves southward along the coast, and the wind is mainly aligned along shore, favoring the southwest direction. Under southerly winds, the ice as a whole does not tend to change directions. In most cases, when the turning angle is close to -180°, the wind direction is southerly (not shown). The highest variability in turning angles and drift speed ratios is at low wind speeds. As the wind speeds increase they come to dominate control of ice drift over the ocean currents.

For comparison with IFT, we downsample the buoy drift trajectories to the 00:00 UTC observations, the approximate time of the MODIS daytime overpass, and re-calculate velocity from daily displacements. Empirical distributions of θ and α for the period from July 15th onward are shown in Figure 3. This period is when the majority of the MOSAiC array is within the region sampled by IFT. Due to the relatively small sample size, the buoy-derived distribution is less evenly sampled than the IFT distribution, yet we see that the main features are reproduced. At wind speeds lower than 7.5 m/s, we are much more likely to see high variability in both the turning angle and in the drift speed ratio. Drift speed ratios at high wind speeds are higher in the buoy data than in IFT, which may be due to differences in spatial sampling. As seen in Figure 3, panel b, the

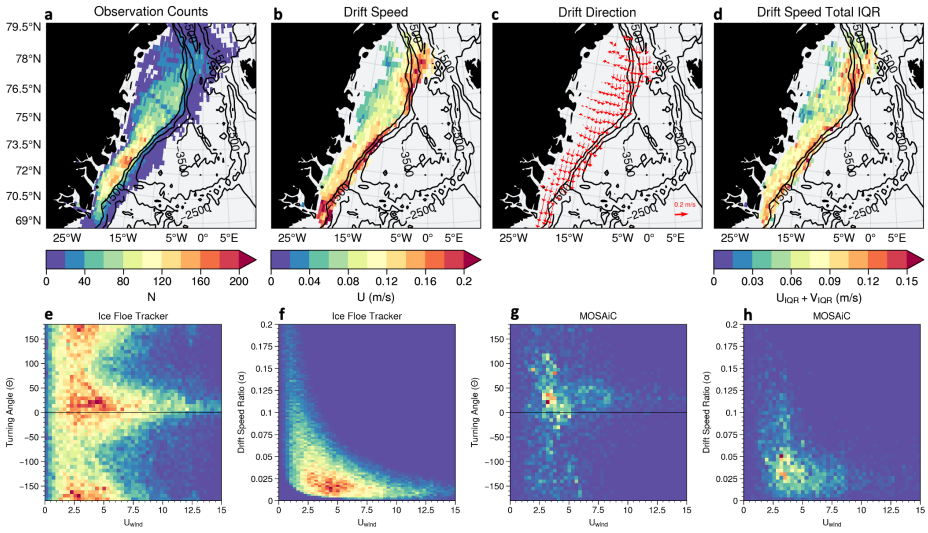

Figure 3. Top row: IFT results binned to a 0.25° latitude by 0.5° longitude grid. (a) Number of observations (b) Median drift speed within each grid cell (c) Median drift direction (d) Sum of the interquartile ranges of zonal and meridional drift velocity. Bottom row: empirical estimates of the joint distributions of ERA5 wind speed and (e) IFT observations of turning angles (f) IFT observations of drift speed ratios (g) MOSAiC observations of turning angles (h) MOSAiC observations of drift speed ratios.

highest median drift speeds are found along the shelf break and within the East Greenland Channel, where many of the buoys were located.

5 Sub-daily sea ice variability, inertial oscillations, and tides

We now quantify the apparent tide-like oscillation seen in Figure 1. The Yermak Plateau and the northern portion of the East Greenland continental shelf are known to be regions with strong tidal currents (Padman et al., 1992; Padman & Erofeeva, 2004; Fer et al., 2015; Luneva et al., 2015). We select 20-day segments of buoy trajectories from four distinct bathymetric regions: the Nansen Basin (NB), the Yermak Plateau (YP), East Greenland Channel (GC), and East Greenland Shelf (GS) (Figure 4a). Rotary spectra show distinct characteristics, with strong signals in both semi-diurnal and diurnal frequency bands everywhere except the deep Nansen Basin (Figure 4, b-e) indicating that tidal currents play an important role in sub-daily sea ice velocity variability. In the northern hemisphere, inertial oscillations are clockwise (CW), which manifests as higher spectral power in the CW direction than in the counterclockwise (CCW). The peak in the semidiurnal band for the Nansen Basin trajectories is small but exists in both CW and CCW components. This suggests the possibility of tidal effects on ice motion even in pack ice well away from the shelves. We note as a topic for future research that the the east-west velocity component displays a regular semi-diurnal oscillation that is not apparent in the north-south velocity component.

The spread of spectral power across the array (indicated by the shading and dotted lines in Figure 4) is smaller in the NB and YP than in the channel and shelf, reflecting both the coherence expected in pack ice and the area sampled. The CCW semi-diurnal peak is narrow and strong in the GC suggesting a clearer influence of semi-diurnal tides.

Over the GS, the diurnal band is no longer distinct, while the semi-diurnal CW band remains strong but increases in spread. Since the shelf region includes a wider range of buoy locations, it is possible that interacting tidal waves and varied bottom topography dilute the tidal signal. Sensor failure and sensor retrieval results in a smaller sample size (26 buoys) representing a region nearly twice as large as the region sampled over the YP, further contributing to the spread in the spectral peak.

The harmonic model assumes that hourly velocity anomalies occur at a limited set of tidal frequencies. When the harmonic model performs well, we interpret that the sub-daily sea ice velocity is consistent with tidal forcing. Tidal constituents are typically estimated from measurements of ocean currents or sea surface height, not sea ice motion; we expect that the additional variability due to imperfect momentum transfer between the surface current and the motion of the ice pack will make the estimate of tidal variability more uncertain. It is therefore notable that we find such strong tidal signals in the ice motion. Implied maximum currents of between 0.1 m/s and 0.2 m/s are seen over the shelf, channel, and plateau, consistent with other tidal current speed estimates (Padman & Erofeeva, 2004; Padman et al., 1992; Vasulkar et al., 2022). These speeds are close to the total drift velocity, hence, tidal currents are likely a major component of ice motion in these regions. For the Yermak Plateau, more than 80% of the sub-daily variance is explained by the tidal currents. The strong change in ocean forcing from the Nansen Basin onto the Yermak Plateau implies a sharp gradient in the ice velocity, inducing deformation. This is confirmed in Figure 1, where we see diurnal oscillation in both divergence and maximum shear that coincides with arrival of the MOSAiC array at the edge of Yermak Plateau.

Inertial oscillations are difficult to differentiate from semi-diurnal tidal variability at high latitudes. Not only are individual semi-diurnal tidal components very close to the inertial period, but tidally generated waves can become inertially trapped. Confidence that the semi-diurnal cycles can be attributed to tides comes from the relatively long 20-day time window used for estimating tidal constituents, and the presence of strong peaks in the CCW band of the rotary spectra. The presence of inertial oscillations in addition to the tidal variability is indicated by the strong CW peaks in the rotary spectra as well as the timing of increases in sub-daily velocity anomalies following brief periods of strong winds, such as occurred on August 15th.

6 Discussion and conclusion

Our results show that sea ice in the East Greenland marginal ice zone is subject to abrupt changes in dominant forcings. We presented evidence of gradients in ocean currents affecting ice dynamics, including strong tidal currents in shallow seas and locally enhanced drift speeds due to shelf boundary currents. As a result of strong ocean forcing, wind direction is a less effective predictor of ice drift in the marginal ice zone.

The MOSAiC ice drift observations capture a broad range of summer ice dynamics in a historically undersampled region. We identify four main regimes of ice motion during the MOSAiC summer drift, with transitions occurring approximately at June 15th, July 13th, and July 26th. Before June 15th, the array is in pack ice, deformation is mainly associated with strong wind events, and the drift speed ratio and turning angles are typical of the central Arctic. The next regime occurs over the Yermak Plateau. There, trajectories are strongly influenced of tidal variability. Gradients in velocity due to the abrupt transition between the basin and tidally active plateau impose strain on the ice, enhancing deformation. The July 13th transition occurs as the array reaches the Greenland Channel, wind speeds drop, and the array begins to accelerate southward. Due to loosening ice pack and low winds, the acceleration is likely due to the array being carried by a strong southward current. The position of the shelf edge constrains the location of the East Greenland Current, which in turn induces shear in the sea ice as the ice pack drifts through

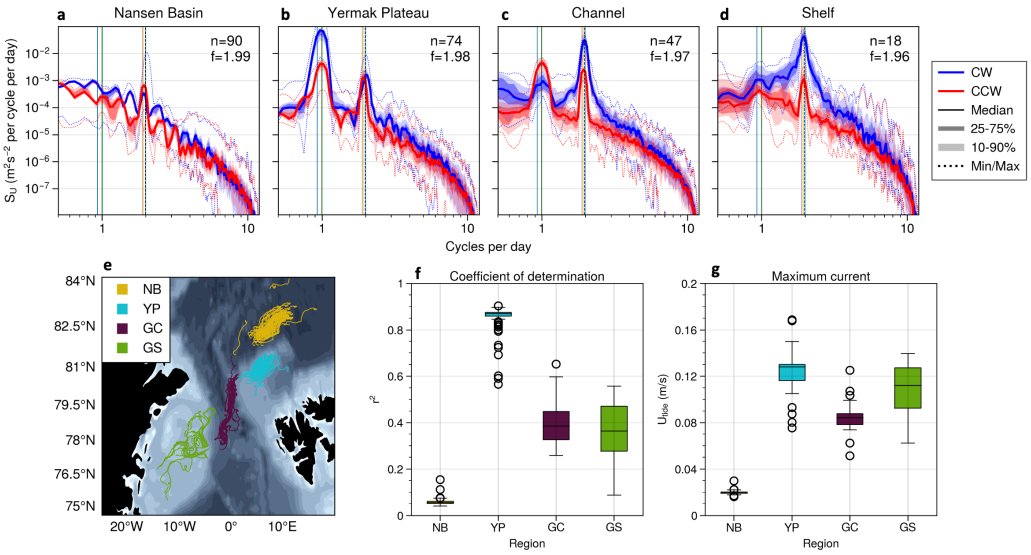

Figure 4. Top: Periodograms of rotary spectra for (a) the Nansen Basin (NB), (b) Yermak Plateau (YP), (c) East Greenland Channel (GC), and the (d) East Greenland Shelf (GS). Dotted lines show the minimum and maximum across the n trajectories. Shading and solid lines show percentile estimates of distributions and the median, respectively. Blue indicates clockwise rotation and red indicates counterclockwise rotation. Bottom, from left to right: (e) Trajectory segments used for frequency analysis (colored by region), (f) box-and-whisker plot of the coefficient of determination (percent variance explained) and (g) box-and-whisker plot of the daily maximum tidal current.

the Fram Strait. After July 26th, we see intermittent wind events, decreasing and decaying sea ice cover, and the buoys disperse across the shallow Greenland Shelf. The increasing wind speed after the buoys leave the Greenland Channel results in a better fit to the wind-driven model (Eq. 2), with decreasing influence of ocean currents on the ice drift.

Transitions between dynamical regimes involve the combination of seasonal decreases in ice concentration, synoptic wind conditions, and spatial variation in ocean currents. Light winds and low ice concentration results in ice motion that follows ocean currents. Drift trajectories have a strong stochastic component due to the interaction of highly variable wind and ocean forcing. The particular path taken by the MOSAiC observatory resulted in a month-long residence over the tidally active Yermak Plateau, enhancing the contrast in the character of variability as the array left the plateau and entered the East Greenland Current.

Low ice concentration late in the summer resulted in the MOSAiC observatory being more sensitive to changes in atmosphere and ocean forcing, unconstrained by internal ice stresses. The wide range of observed turning angles and drift speeds indicate an important role for ocean variability. As we showed through the IFT drift statistics, such variability is not limited to the MOSAiC observational period for the Greenland Shelf region, but is a typical feature of this highly dynamic region.

Models of sea ice drift that fail to take mesoscale ocean variability and tides into account will systematically underestimate drift variability and deformation. Furthermore, remote sensing observations with spatial resolutions too low to capture transitions between ocean current systems and temporal resolutions too low to capture tides will systematically underestimate sea ice deformation. Use of a tidal model to supplement sea ice motion vectors may offer a path forward for improving estimates of sea ice deformation in coastal and shallow seas.

7 Open Research

MOSAiC drift tracks are freely available from the Arctic Data Center (Bliss et al., 2022). 10m wind data from ERA5 is available at the Copernicus Data Store (Hersbach et al., 2018). IBCAO bathymetric data at 400 m by 400 m resolution was downloaded from `https://www.gebco.net/data_and_products/gridded_bathymetry_data/arctic_ocean/`. Ice Floe Tracker trajectories, derived data and code used for this analysis are available at `https://github.com/danielmwatkins/evidence_of_abrupt_transitions`. The final version of the code will be archived at Zenodo.

We acknowledge the use of MODIS True Color Corrected Reflectance imagery from the Terra and Aqua satellites aquired via the from the Worldview Snapshots application (https://wvs.earthdata.nasa.gov), part of the Earth Observing System Data and Information System (EOSDIS).

Analysis was carried out using the open source Python scientific computing stack, and we wish to acknowledge the contributions of volunteer developers who maintain and develop this resource. Data analysis was performed using xarray (Hoyer & Hamman, 2017), pandas (pandas development team, 2020), NumPy (Harris et al., 2020), and SciPy (Virtanen et al., 2020). Figures were prepared using the ProPlot Python library (Davis, 2021).

Acknowledgments
DW, JH, and MMW were supported by NASA The Science of Terra, Aqua, and Suomi-NPP Program (20-TASNPP20-0202). DW and JH were also supported by a grant from the Department of Energy Atmospheric Systems Research. AB, DW, and JH were supported by the National Science Foundation grant 1722729. AB was supported by NASA's

Internal Scientist Funding Model in the Cryospheric Sciences Laboratory. MW was supported by grants from the Office of Naval Research (ONR) Arctic Program (N00014-20-1-2753) and the ONR Multidisciplinary University Research Initiatives Program (N00014-22-1-2722).

Drift track data used in this manuscript was produced as part of the international Multidisciplinary drifting Observatory for the Study of the Arctic Climate (MOSAiC) with the tag MOSAiC20192020 and the Project_ID: AWI_PS122_00. The authors acknowledge the data collection and processing efforts of the MOSAiC science and logistics teams and of all those who contributed to MOSAiC and made this endeavour possible (Nixdorf et al. 2021).

The authors declare no conflicts of interest.

References

Bliss, A. C., Hutchings, J. K., Anderson, P., Anhaus, P., & Belter, H. J. (2022). *Sea ice drift tracks from the Distributed Network of autonomous buoys deployed during the Multidisciplinary drifting Observatory for the Study of Arctic Climate (MOSAiC) expedition 2019-2021.* Arctic Data Center. Retrieved from `https://arcticdata.io/catalog/view/urn%3Auuid%3A56ffc86a-ddea-4379-a27a-09c992e65f16`

Boylan, B. M. (2021, September). Increased maritime traffic in the Arctic: Implications for governance of Arctic sea routes. *Marine Policy*, *131*, 104566. doi: 10.1016/j.marpol.2021.104566

Brunette, C., Tremblay, L. B., & Newton, R. (2022). A new state-dependent parameterization for the free drift of sea ice. *Cryosphere*, *16*(2), 533–557. doi: 10.5194/tc-16-533-2022

Comiso, J. C., Meier, W. N., & Gersten, R. (2017). Variability and trends in the Arctic Sea ice cover: Results from different techniques. *Journal of Geophysical Research: Oceans*, *122*(8), 6883–6900. doi: 10.1002/2017JC012768

Davis, L. L. B. (2021, October). *Proplot.* Zenodo. Retrieved from `https://doi.org/10.5281/zenodo.5602155` doi: 10.5281/zenodo.5602155

Dawson, J., Pizzolato, L., Howell, S. E., Copland, L., & Johnston, M. E. (2018, February). Temporal and Spatial Patterns of Ship Traffic in the Canadian Arctic from 1990 to 2015 + Supplementary Appendix 1: Figs. S1–S7 (See Article Tools). *ARCTIC*, *71*(1). doi: 10.14430/arctic4698

Dumont, D. (2022, October). Marginal ice zone dynamics: History, definitions and research perspectives. *Philosophical Transactions of the Royal Society A: Mathematical, Physical and Engineering Sciences*, *380*(2235), 20210253. doi: 10.1098/rsta.2021.0253

Feldl, N., Po-Chedley, S., Singh, H. K., Hay, S., & Kushner, P. J. (2020). Sea ice and atmospheric circulation shape the high-latitude lapse rate feedback. *npj Climate and Atmospheric Science*, *3*(1), 1–9. doi: 10.1038/s41612-020-00146-7

Fer, I., Müller, M., & Peterson, A. K. (2015, March). Tidal forcing, energetics, and mixing near the Yermak Plateau. *Ocean Science*, *11*(2), 287–304. doi: 10.5194/os-11-287-2015

Harris, C. R., Millman, K. J., van der Walt, S. J., Gommers, R., Virtanen, P., Cournapeau, D., ... Oliphant, T. E. (2020, September). Array programming with NumPy. *Nature*, *585*(7825), 357–362. Retrieved from `https://doi.org/10.1038/s41586-020-2649-2` doi: 10.1038/s41586-020-2649-2

Hatcher, S., Ahmed, A., Kim, M., & Wilhelmus, M. M. (2022, April). *SOIT: Satellite overpass identification tool.* Zenodo. Retrieved from `https://doi.org/10.5281/zenodo.6475619` doi: 10.5281/zenodo.6475619

Heil, P., Hutchings, J. K., Worby, A. P., Johansson, M., Launiainen, J., Haas, C.,

& Hibler, W. D. (2008, April). Tidal forcing on sea-ice drift and deformation in the western Weddell Sea in early austral summer, 2004. *Deep Sea Research Part II: Topical Studies in Oceanography*, *55*(8-9), 943–962. doi: 10.1016/j.dsr2.2007.12.026

Hersbach, H., Bell, B., Berrisford, P., Biavati, G., Horányi, A., Muñoz Sabater, J., ... Thépaut, J.-n. (2018). *ERA5 hourly data on single levels from 1959 to present.* Copernicus Climate Change Service (C3S) Climate Data Store (CDS). doi: 10.24381/cds.adbb2d47

Hersbach, H., Bell, B., Berrisford, P., Hirahara, S., Horányi, A., Nicolas, J., ... Thépaut, J.-n. (2020). The ERA5 global reanalysis. *Quarterly Journal of the Royal Meteorological Society*, 1999–2049. doi: 10.1002/qj.3803

Hoyer, S., & Hamman, J. (2017, April). Xarray: N-D labeled Arrays and Datasets in Python. *Journal of Open Research Software*, *5*(1), 10. doi: 10.5334/jors.148

Hutchings, J. K., Heil, P., Steer, A., & Hibler, W. D. (2012). Subsynoptic scale spatial variability of sea ice deformation in the western Weddell Sea during early summer. *Journal of Geophysical Research*, *117*(C1), C01002. doi: 10.1029/2011JC006961

Hutchings, J. K., Roberts, A., Geiger, C. A., & Richter-Menge, J. (2011). Spatial and temporal characterization of sea-ice deformation. *Annals of Glaciology*, *52*(57 PART 2), 360–368. doi: 10.3189/172756411795931769

Hutchings, J. K., Roberts, A., Geiger, C. A., & Richter-Menge, J. (2018). Corrigendum: Spatial and temporal characterisation of sea-ice deformation. *Journal of Glaciology*, *64*(244), 343–346. doi: 10.1017/jog.2018.11

Jakobsson, M., Mayer, L. A., Bringenspar, C., Castro, C. F., Mohammad, R., Johnson, P., ... Zinglersen, K. B. (2020). The International Bathymetric Chart of the Arctic Ocean Version 4.0. *Scientific Data*, *7*(176), 14.

Krumpen, T., & Sokolov, V. (2020). *The Expedition AF122/1 Setting up the MOSAiC Distributed Network in October 2019 with Research Vessel Akademik Fedorov* (Tech. Rep. No. October 2019). Potsdam, Germany: Alfred Wegener Institute.

Kwok, R. (2010). Satellite remote sensing of sea-ice thickness and kinematics: A review. *Journal of Glaciology*, *56*(200), 1129–1140. doi: 10.3189/002214311796406167

Lopez-Acosta, R., Schodlok, M. P., & Wilhelmus, M. M. (2019). Ice Floe Tracker: An algorithm to automatically retrieve Lagrangian trajectories via feature matching from moderate-resolution visual imagery. *Remote Sensing of Environment*, *234*(October), 111406. doi: 10.1016/j.rse.2019.111406

Luneva, M. V., Aksenov, Y., Harle, J. D., & Holt, J. T. (2015). The effects of tides on the water mass mixing and sea ice in the Arctic Ocean. *Journal of Geophysical Research: Oceans*, *120*, 6669–6699. doi: 10.1038/175238c0

Manucharyan, G. E., Lopez-Acosta, R., & Wilhelmus, M. M. (2022). Spinning ice floes reveal intensification of mesoscale eddies in the western Arctic Ocean. *Scientific Reports*, *12*(7070).

Maslanik, J. A., Fowler, C., Stroeve, J., Drobot, S., Zwally, J., Yi, D., & Emery, W. (2007). A younger, thinner Arctic ice cover: Increased potential for rapid, extensive sea-ice loss. *Geophysical Research Letters*, *34*(24), 2004–2008. doi: 10.1029/2007GL032043

Meier, W. N., T. M., & Comiso., J. C. (2018). *AMSR-E/AMSR2 unified L3 daily 12.5 km brightness temperatures, sea ice concentration, motion & snow depth polar grids, version 1.* NASA National Snow and Ice Data Center Distributed Active Archive Center. doi: 10.5067/RA1MIJOYPK3P

Nicolaus, M. (2022). Overview of the MOSAiC expedition: Snow and sea ice. *Elementa: Science of the Anthropocene*, *9*(1). doi: 10.1525/elementa.2021.000046

Padman, L., & Erofeeva, S. (2004, January). A barotropic inverse tidal

model for the Arctic Ocean. *Geophysical Research Letters*, *31*(2). doi: 10.1029/2003GL019003

Padman, L., Plueddemann, A. J., Muench, R. D., & Pinkel, R. (1992). Diurnal tides near the Yermak Plateau. *Journal of Geophysical Research*, *97*(C8), 12639. doi: 10.1029/92JC01097

pandas development team, T. (2020, February). *Pandas-dev/pandas: Pandas.* Zenodo. doi: 10.5281/zenodo.3509134

Pease, C. H., Turet, P., & Pritchard, R. S. (1995). Barents Sea tidal and inertial motions from Argos ice buoys during the Coordinated Eastern Arctic Experiment. *Journal of Geophysical Research*, *100*(C12), 24705. doi: 10.1029/95JC03014

Polyakov, I. V., Rippeth, T. P., Fer, I., Baumann, T. M., Carmack, E. C., Ivanov, V. V., ... Rember, R. (2020, August). Intensification of Near-Surface Currents and Shear in the Eastern Arctic Ocean. *Geophysical Research Letters*, *47*(16). doi: 10.1029/2020GL089469

Quadfasel, D., Gascard, J.-C., & Koltermann, K.-P. (1987). Large-scale oceanography in Fram Strait during the 1984 Marginal Ice Zone Experiment. *Journal of Geophysical Research*, *92*(C7), 6719. doi: 10.1029/JC092iC07p06719

Richter, M. E., von Appen, W.-J., & Wekerle, C. (2018, September). Does the East Greenland Current exist in the northern Fram Strait? *Ocean Science*, *14*(5), 1147–1165. doi: 10.5194/os-14-1147-2018

Taylor, P. C., Boeke, R. C., Boisvert, L. N., Feldl, N., Henry, M., Huang, Y., ... Tan, I. (2022, February). Process Drivers, Inter-Model Spread, and the Path Forward: A Review of Amplified Arctic Warming. *Frontiers in Earth Science*, *9*, 758361. doi: 10.3389/feart.2021.758361

Thorndike, A., & Colony, R. (1982). Sea ice motion in response to geostrophic winds. *Journal of Geophysical Research*, *87*(C8), 5845–5852.

Vasulkar, A., Verlaan, M., Slobbe, C., & Kaleschke, L. (2022, August). Tidal dissipation from free drift sea ice in the Barents Sea assessed using GNSS beacon observations. *Ocean Dynamics*, *72*(8), 577–597. doi: 10.1007/s10236-022-01516-w

Virtanen, P., Gommers, R., Oliphant, T. E., Haberland, M., Reddy, T., Cournapeau, D., ... SciPy 1.0 Contributors (2020). SciPy 1.0: Fundamental algorithms for scientific computing in python. *Nature Methods*, *17*, 261–272. doi: 10.1038/s41592-019-0686-2